

Two Optimized Hexapod Leg Designs with Improved Hysteresis for a Hybrid Testing Application

Wikkerink, M.T.



Master's Thesis

Two Optimized Hexapod Leg Designs with Improved Hysteresis for a Hybrid Testing Application

July 2025

By Marc Wikkerink
Born on the 22th of August 2001
in Doetinchem, the Netherlands

Examination committee:
prof.dr.ir. D.M. Brouwer EngD
dr.ir. K.S. Dwarshuis
dr.ir. M. Nijenhuis
dr.ir. R.G.K.M. Aarts
B. Gerlagh MSc

University of Twente
Faculty of Engineering Technology
Precision Engineering

Two Optimized Hexapod Leg Designs with Improved Hysteresis for a Hybrid Testing Application

Abstract: In precision applications, hysteresis often results in significant performance limitations. In this paper, two hexapod leg designs with minimized hysteresis are presented. The research is used to determine a suitable design direction for a next-generation hybrid testing setup for offshore floating wind turbines. Two actuator layouts are considered: an arc-based design including flexures, and a linear design utilizing air bearings. To address the dominant contribution of moving power cables induced hysteresis, cables are partially replaced with deterministic compliant elements. A two-linkage cable guide is developed and moving-coil configurations are implemented. This enables the use of ironless core actuators, which result in low hysteresis and cogging-free operation, while still meeting the tight requirements on the moving mass, actuation forces, and hysteresis. Experimental validation shows a maximum hysteresis of 0.0083 Nm for the arc design and 0.037 N for the linear design, corresponding to 0.0233% and 0.0319% of their respective continuous torque or force ratings. Compared to a hexapod with iron core actuators (the T-Flex), the arc and linear designs reduce the hysteresis to 3.4% and 4.7%, respectively. With this achievement, the performance limitations by hysteresis are effectively eliminated, as the hysteresis will no longer be the critical factor in the current designs. The findings presented in this paper demonstrate significant progress in improving hexapod precision and provide a foundation for future development of hybrid testing platforms for offshore renewable energy systems.

Keywords: 6-DOF manipulator, Force transparency, Cable slab, Compliant mechanisms, Air bearings

1 Introduction

1.1 Background

The energy transition demands new innovative solutions for renewable energy. Renewable energy can be obtained from various sources, such as wind energy, which is harnessed by wind turbines. Locating these wind turbines offshore poses several advantages, such as the available offshore area and stronger, and more consistent wind [1]. However, the installation cost for offshore wind turbines is significantly higher than for onshore turbines. Moreover, the maximum water depth for fixed foundation wind turbines is limited. Offshore floating wind turbines counteract these drawbacks.

Advancing the development of floating offshore wind turbines requires a thorough understanding of their complex aerodynamic and hydrodynamic behavior, which relies on experimental data. This data is obtained in a financially efficient manner using scaled model wind turbines during testing. Testing floating wind turbines is particularly challenging due to the inherent coupling between aerodynamic and hydrodynamic effects.

Representative testing relies on proper scaling of length relative to the characteristic velocity to maintain similarity, and accurately replicate real-

world physical conditions. To maintain aerodynamic similarity, the Reynolds number must be representative, whereas for hydrodynamic behavior, the Froude number should match that of the actual system. Since the scaling requirements for these two domains differ, it is generally not feasible to satisfy both simultaneously [2].

To overcome this limitation, hybrid testing—also known as hybrid-in-the-loop (HIL)—has been proposed. In hybrid testing, the aerodynamic and hydrodynamic domains are decoupled by numerically simulating one domain while physically testing the other. Figure 1 provides a schematic representation of a hybrid testing setup, in which the aerodynamic domain is physically tested. This approach eliminates the need to satisfy the scaling requirement of the numerically simulated domain, as it is not physically represented.

HybridLabs, the consortium that commissioned this research, is initiated to accelerate offshore renewable energy innovation. The consortium was launched in 2024 with the vision of building a unique infrastructure comprising hybrid experimental facilities and offshore demonstration sites, driven by physics- and data-driven approaches [3]. Their objective is to enable cost-effective development of floating wind and hydrogen technologies.

Figure 2 provides one of HybridLabs' current

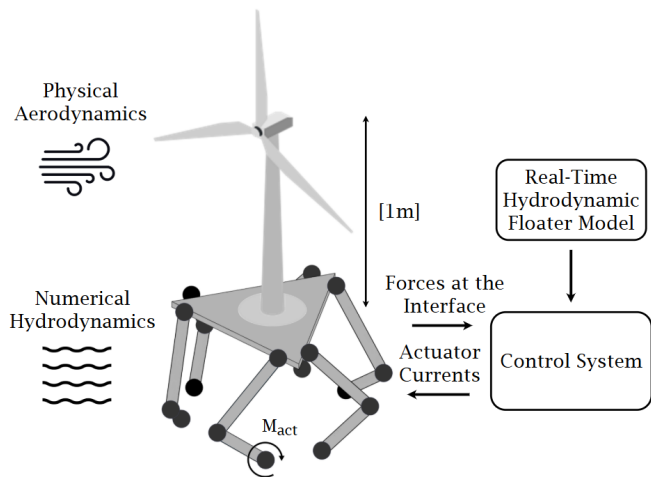


Figure 1: Schematic visualization of the hybrid testing setup

hybrid testing setups. The setup is placed inside a wind tunnel, while a six degree of freedom manipulator represents the dynamic behavior of the floating platform, to physically test the aerodynamic behavior of the wind turbine. To improve the quality of the test data, a more accurate representation of the floating platform is required. The numerical model should match the dynamical behavior of the floating platform of the wind turbine, which sets demanding requirements on the moving mass.

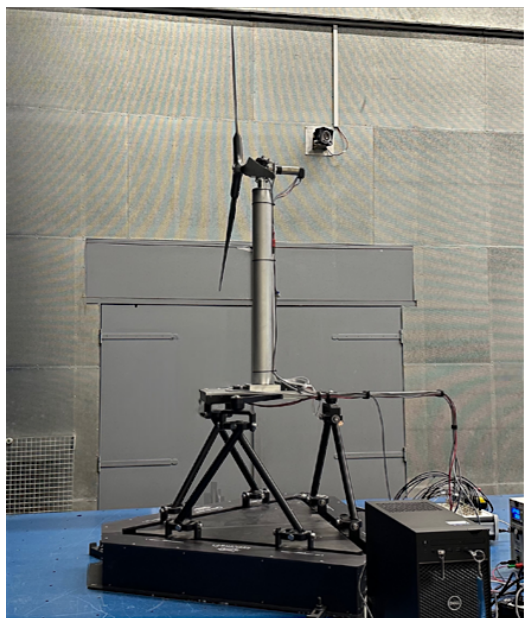


Figure 2: One of HybridLabs' hybrid testing setup

A high force transparency between the end-effector and actuators is required in order to apply the new control strategy. The force exerted on the hexapod is used in the control loop to match the dynamic response of the platform; this is known as interaction control. In the envisioned system, the forces at the interface—exerted on the hexapod

by the wind turbine—will be calculated using the actuator currents. Hysteresis between the actuator and the end-effector, therefore, results in an uncertainty in the calculated force. To enable the effective implementation of the envisioned interaction control, hysteresis must be further reduced.

A hexapod—a six-degree-of-freedom (6-DOF) parallel robot—is well-suited for this application due to its low moving mass, primarily because the actuators can be mounted on the fixed base. By incorporating flexures or air bearings—which eliminate friction and backlash, and provide highly deterministic behavior—high force transparency can be achieved. These characteristics render a hexapod with low-friction elements suitable for the numerical structure required in hybrid testing of floating wind turbines.

1.2 Objectives

This paper aims to improve the performance of a next-generation large-range-of-motion hexapod, by minimizing the hysteresis. It presents two designs for a hexapod leg, aiming for low moving mass and low hysteresis. One design includes an arc motor guided by flexures; the second incorporates a linear actuator guided by air bearings. The moving-coil configurations demand adequate cable routing to achieve a low hysteresis. These two potential solutions serve as a preliminary study, with the goal of determining the design direction for a new hybrid testing setup.

1.3 Outline

First, in Section 2, the requirements for the complete hexapod are listed. Section 3 provides the conceptual design solutions, including a parametric representation. The design parameters are obtained through multi-body optimization, as described in Section 4. In Section 5, the final designs for the test setups are presented. The designs are validated by the system identifications and hysteresis tests, in Section 6. Section 7 discusses the obtained test results. Finally, in Section 8, the conclusions of this research are presented.

2 Requirements

2.1 Overview

The hybrid testing application demands a hexapod with a large range of motion, low hysteresis, and a low equivalent mass while achieving high accelerations. Table 1 lists the targeted specifications for the entire hexapod. These targeted spec-

ifications are based on simulations on the IEA 15 Megawatt reference wind turbine, performed using OpenFAST software. The results are scaled with a length scale of 160 and a velocity scale of 3. The requirements relate to the coordinate frame represented in Figure 3.

Parameter	Specification
Motion	
Translational displacement x,y	+/- 105 [mm]
Translational displacement z	+/- 56 [mm]
Rotational displacement x,y	+/- 8 [deg]
Rotational displacement z	+/- 3 [deg]
Translational velocity x,y,z	0.35 [m/s]
Rotational velocity x,y,z	35 [deg/s]
Translational acceleration x,y,z	15 [m/s ²]
Rotational acceleration x,y,z	1500 [deg/s ²]
Equivalent mass at end-effector	
Equivalent mass in x,y	<2.36 [kg]
Equivalent mass in z	<6.06 [kg]
Other	
Hysteresis	<1 [N]
Load (placed at 1 m vertical distance)	2.5 [kg]
First parasitic eigenfrequency	>50 [Hz]

Note: The requirements on displacement, velocity and acceleration are all independent in combination with the load. Additionally, for the displacements, velocities, and accelerations, hold that half of the magnitude of all the independent displacements must be able to be reached simultaneously.

Table 1: The requirements for the entire Hexapod

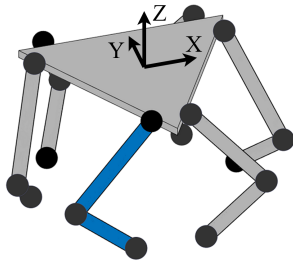


Figure 3: Visualization of the hexapod coordinate frame, with the leg whose local frame matches the global frame shaded in blue

2.2 Equivalent Mass

The stability criteria of the plant and controller limit the maximum equivalent mass of the hexapod. The controller transforms the dynamic behavior of the hexapod to obtain the desired model that simulates the floating platform. Stability issues arise if the virtual controller mass becomes negative, which occurs when the plant mass (equivalent mass of the hexapod) is larger than the desired

mass. As a result, strict mass requirements apply to the hexapod. However, damping from the hydrodynamic floater model could significantly relax this restriction. Nonetheless, the worst case, where the equivalent hexapod mass is equal to the virtual controller mass, is taken into account.

The requirements on the equivalent moving mass arise from the mass of the desired model, which are the scaled down inertia's of the platform. Since the dynamics must be matched to the inertia's of the platform at the interface to the wind turbine, the mass requirement relates to the equivalent moving mass evaluated at the end-effector of the hexapod. The desired length scaling of the wind turbine is $\lambda_L = 160$, resulting in an inertia scaling of $\lambda_I = 160^3$. The scaled inertia's can be found in Table 2

Target Mass	Full Model	Scaled Model
Surge	9.66×10^6	2.36 [kg]
Sway	9.66×10^6	2.36 [kg]
Heave	2.48×10^7	6.06 [kg]
Roll	2.41×10^1	0.23 [kgm ²]
Pitch	2.41×10^1	0.23 [kgm ²]
Yaw	4.38×10^1	0.42 [kgm ²]

Table 2: Comparison of target mass values, for full and scaled models

2.3 Natural Frequencies

The control bandwidth of the hexapod is limited by the first parasitic eigenfrequency. The required control bandwidth of the hexapod is 10 Hz. As a rule of thumb, the first parasitic eigenfrequency must be at least a factor of five higher than the required control bandwidth. As a result, the first parasitic eigenfrequency must exceed 50 Hz. A one-leg model is derived to translate the eigenfrequency requirement on the entire hexapod to a single leg, which is discussed in more detail in Section 4.1.1.

2.4 Driving forces

The required driving force of a single leg in the axial direction of the upper arm is specified at 100 N in combination with an end-effector radius of 0.4 m. The driving force is determined by the required driving torque to satisfy the required rotational acceleration of the end-effector. Consequently, the driving force is inversely proportional to the end-effector radius. The requirement is based on simulations of a complete hexapod, under preliminary design choices and estimations for inertias.

3 Conceptual Design

In this section, two solutions for the design problem are presented: the 'arc concept' and the 'linear concept'. Concept solutions are selected based on a combination of estimated performance and the opportunity to gather useful information.

3.1 Actuators

The actuators play a key role in shaping the overall design of the leg and significantly impact the performance of the system. The hexapod requires actuators with low mass, high actuation force, and low hysteresis. To achieve low-hysteresis actuation, transmission components are eliminated employing direct-drive actuators.

Voice coil actuators are very well-suited direct-drive actuators for precision applications. Due to the absence of commutation, voice coil actuators achieve very smooth motion. However, voice coil actuators are very limited in stroke—typically <25 mm—which is insufficient for the intended application, eliminating this type of non-commutating actuation. Consequently, commutating actuators are considered, available in both iron-core and ironless-core configurations.

Commutating actuators with an iron core are avoided, despite the high torque density, these actuators pose at least four significant drawbacks. Firstly, the interaction between the permanent magnets and iron core results in a position-dependent torque even without an applied current, affecting the smoothness of the motion due to cogging effects. Secondly, the interaction between the permanent magnets and the iron core introduces a negative stiffness which is dependent on the misalignment of the rotor, increasing the complexity of the actuator support [4]. Thirdly, periodic magnetization and demagnetization of the iron core results in magnetic hysteresis, seriously affecting precision. Lastly, iron-core motors do not maximize the opportunity to gather useful information, as the performance of an iron-core direct-drive torque motor in a precision large-stroke hexapod is already well documented [5].

Taking all aspects into account, ironless commutation actuators are selected. The actuator of choice for the rotational arc design is the IL91C-9 from Suzhou ITG Linear Motor Co. The IL91C-9 can deliver a maximum continuous torque of 35.5 Nm [6]. For the linear concept, the linear ironless actuator of the UM12 series of Tecnotion is selected. The UM12 is capable of delivering a continuous force of 116 N [7]. The selected actuators have the lowest moving mass in relation to the continuous torque

and force ratings compared to competitors.

Both actuators consist of a coil unit and a yoke with permanent magnets. Implementation options include moving-coil and moving-magnet configurations. Due to the high weight of these yokes (1.9 kg for the UM12 and 3.2 kg for the IL91C-9), it is inevitable to apply the actuators in a moving-coil configuration. This implies that the actuators move the power cable. A moving cable is undesirable for the hysteresis, since moving cables are known for indeterminism. This indeterminism is resolved by adequate cable routing designs, as discussed in Section 5.

3.2 Kinematic structure

In this section, the kinematic structures of the concepts are presented. Concept solutions are selected based on a combination of estimated performance and their potential to yield valuable insights. Accordingly, both linear and rotational kinematic structures are investigated, in combination with flexures and air bearings, in well-suited combinations. During the concept design, a rotational design featuring air bearings was eliminated, as well as an alternative linear configuration. For a more detailed discussion of these concepts, see Appendix A.

3.2.1 Arc concept

The first proposed concept consists of the IL91C-9 ironless arc motor, in combination with a revolute flexure joint at the base. Since the deflections are relatively small, a simple flexure using crossed leaf springs can be implemented. The upper arm consists of two universal joints and a revolute joint to release the remaining DOF, resulting in a 6-RURU hexapod layout. Combining these design choices results in a concept as illustrated in Figure 4.

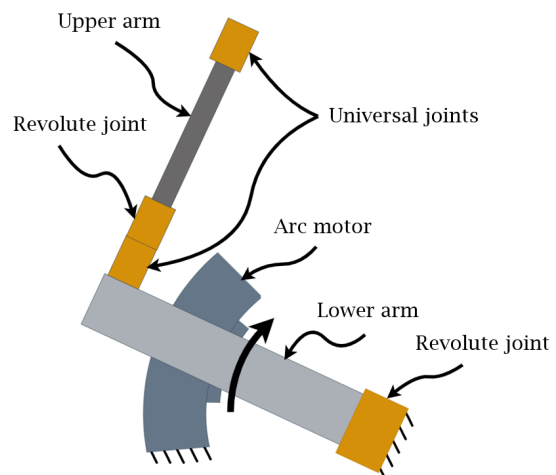


Figure 4: Schematic representation arc concept

3.2.2 Linear concept

Implementing linear motion using flexures leads to large overall dimensions in order to achieve the required range of motion, thereby exceeding the system's mass constraints. Consequently, air bearings are considered more suitable for the linear design, as they can accommodate large ranges of motion without significantly increasing the system's size or mass.

A second concept, depicted in Figure 5, is created by combining the UM12 linear ironless actuator with air bearings to constrain the lower arm. The upper arm also utilizes two universal joints and a revolute joint, creating a 6-PURU layout hexapod.

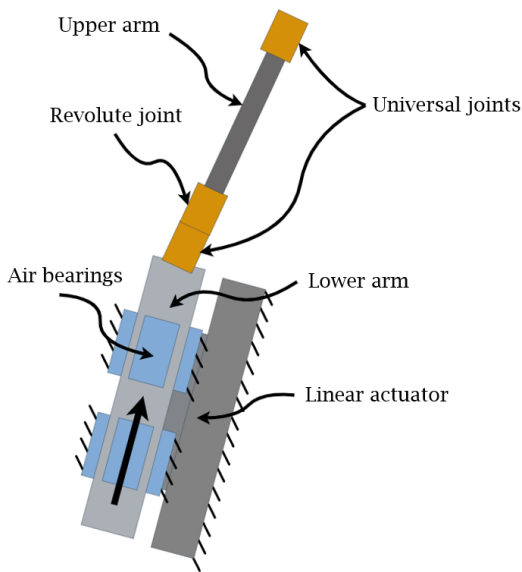


Figure 5: Schematic representation linear concept

3.2.3 Upper arm

As outlined in Sections 3.2.1 and 3.2.2, both concepts employ an identical upper arm configuration, which comprises two universal joints and a revolute joint. The upper arm is not designed in detail, since the effects of the air bearings, actuators, and moving cables are of the highest interest. In addition, proper experimental validation of a complete leg design is less practical. The individual legs have five unconstrained DOF's. In order to perform tests, the legs must be additionally constraint, potentially introducing unwanted hysteresis, distorting the test results. However, in order to perform optimization and prove the concepts are feasible, the upper arm must be defined in sufficient detail.

In [8], a universal joint design is presented which consists of two stacked butterfly revolute joints. This design shows improvement in support stiff-

ness as well as complexity compared to the universal and spherical joints presented in [9], used in the T-Flex. The arm itself will be made of a composite tube, as a lightweight material is required due to the tight equivalent mass constraint and the direct contribution to the equivalent mass. To release the torsional DOF in the upper arm, a revolute flexure joint is added.

3.3 Encoders

Positions are measured by the 1 nm measuring step version of Heidenhain's LIC 4119 encoder. This open linear absolute encoder is also used for the commutation of the actuators. For the arc concept, the linear scale is mounted on a curved surface to measure the angle, resulting in a resolution of 5 nrad.

4 Optimization

For optimal performance, a high first parasitic eigenfrequency is required. The first parasitic eigenfrequency and equivalent mass are functions of all main design parameters, which exhibit strong coupling. Hence, proper manual selection of the parameters is a complex task. To mitigate this issue, a gradient-based optimization is used to maximize the first parasitic eigenfrequency. The first parasitic eigenfrequency is evaluated by modal analysis performed using the flexible multi-body software SPACAR. SPACAR enables modeling the kinematics and dynamics of multi-body systems using analytical formulations for a series of flexible beam elements. Its low computational effort makes SPACAR extremely suitable for running in an optimization loop. To further reduce computational effort, the base flexure of the arc concept is split into a separate optimization, which is discussed in Section 4.4.

4.1 Method

This subsection describes the method of the optimization for the main design parameters.

4.1.1 Load case

Due to the large rotational inertia of the wind turbine load, a rotational mode of the end-effector, as illustrated in Figure 6, is expected to correspond to the first eigenfrequency.

To evaluate the performance of a single leg without modeling the complete hexapod, a one-leg model is formulated. This model provides the

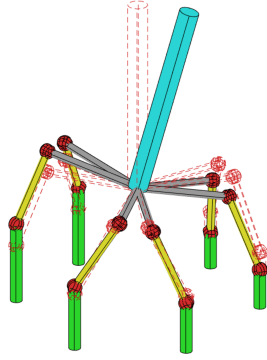


Figure 6: Typical first eigen-mode for the hexapod with a load of 2.5 kg positioned 1 m above the end-effector, joints are visualized in red, actuator assemblies will replace the green elements

equivalent moving mass of the mode shape perceived at the top of the upper arm in the arm's axial direction. The equivalent moving mass in the arm direction is used as the load case in the optimization and is calculated according to the following equation:

$$M_{eq} = \frac{2.5}{(4 \cdot R^2 \cdot \sin^2(60^\circ) \cdot \sin^2(\theta_1))} \quad (1)$$

where R is the end-effector radius and θ_1 is the reference angle of the upper arm. Note that this mass is only valid for this specific eigenmode. Without the connection to the end-effector, the arm has six DOFs. Therefore, five additional constraints are added to allow only for motion in arm's axial direction.

4.1.2 Design constraints

The concepts are optimized under the mass constraints presented in Table 2. Besides the mass constraint, additional constraints are introduced, such as the maximum continuous actuator force or torque. For the arc design, an additional constraint equation prevents collision between the upper arm and the actuator yoke. Without constraints on the stroke of the arc motor, the maximum stroke of 18 degrees of a single yoke is slightly exceeded. To enable the use of a single yoke per leg, a constraint on the stroke is introduced.

4.1.3 Optimization parameters

Although the two concepts have different kinematic structures, they can both be expressed in the same optimization parameters. Table 3 presents these optimization parameters, which correspond to Figures 7a and 7b.

Figure 7 shows the kinematic structure and parametrization of the arc concept in the x-z plane

Parameter	Symbol
Length upper arm	L_1
Reference angle lower arm	θ_2
Length lower arm	L_2
End-effector radius	R

Table 3: Optimization parameters

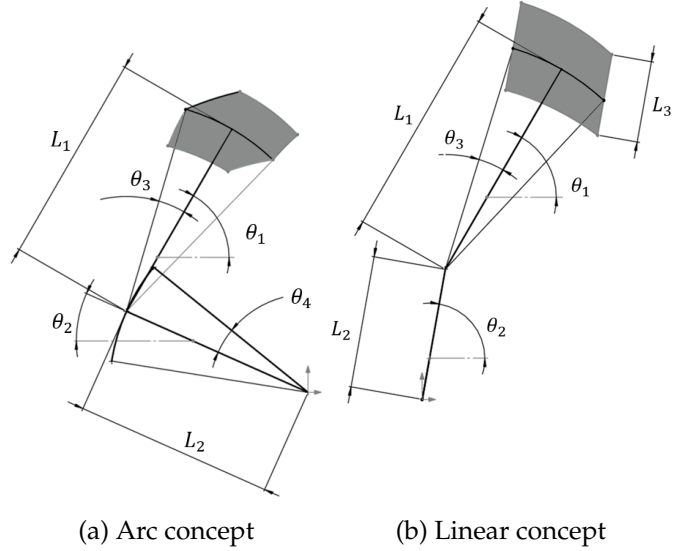


Figure 7: Parametrization of the two concepts

as defined in Figure 3. Where θ_1 and θ_2 are the reference angles of the upper and lower arm respectively. Angle θ_1 is not defined as an optimization parameter, as it is highly dependent on the complete hexapod configuration. Based on simulations conducted on a complete reference hexapod, θ_1 is fixed to 60 degrees. The angles θ_3 and θ_4 represent the deformation angles of the joints. The resulting shape of the range of motion is shaded gray. The deflections of the joints and actuator strokes are calculated to fit the required range of motion. Together with the other parameters, these are used to define the modal SPACAR models.

As discussed in Section 4.1.1, the end-effector radius has a strong impact on the load case and directly affects the equivalent mass and required driving forces. Hence, although the end-effector radius does not parameterize the hexapod leg, it is an important optimization parameter.

The eigenfrequency in the arc concept optimization is evaluated in the reference configuration, incorporating the support stiffness's of the deflected joints. However, applying this method for the linear concept this method will yield an optimal optimization. Specifically, for the condition when θ_2 equals θ_1 , the air bearings are not under load in the reference position. Consequently, the distance between the air bearings does not contribute to the stiffness and eigenfrequency, while minimizing L_2

does reduce the moving mass. As a result, the extreme reduction of L_2 leads to suboptimal eigenfrequencies in configurations deviating from the reference position. To address this limitation, the configurations of the extrema of the range of motion are included the optimization.

4.1.4 Joints

The support stiffness of the universal joints is highly dependent on both the deflection as the maximum stroke, as described by the following equation:

$$K = \left(\frac{0.436}{\beta}\right)^3 \frac{10^6}{0.125 + 4.6\phi^2} \quad (2)$$

Where β is the range of motion and ϕ the deflection angle in radians [8]. In Figure 8 the relation between deflections and support stiffness is plotted.

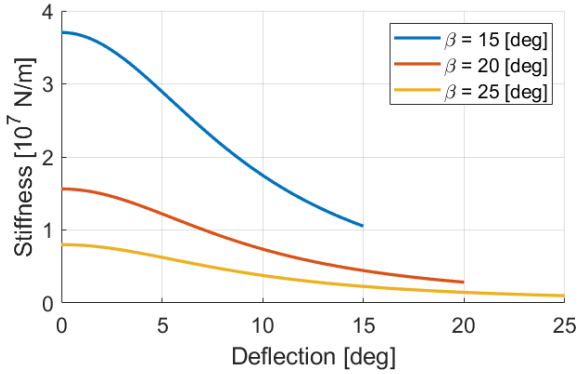


Figure 8: Support stiffness universal joint in relation to range of motion and deflection

The eigenfrequency is evaluated with deflected joint stiffness's. The joint stiffness's are obtained by a separate kinematic SPACAR model which returns all maximum deflection angles for the extrema of the workspace as a function of the optimization parameters. With the deflection angles, the required stroke β is determined for both universal joints. The parameter ϕ is configuration dependent. The support stiffness's for the configurations at the extrema of the range of motion, are then all evaluated with the correct parameters according to equation (2).

4.1.5 Mass

The equivalent mass of a single arm is calculated inside the optimization loop using a dynamic SPACAR model. The end-effector mass is approximated by the following equation:

$$m_{End} = \left(\frac{R}{0.2}\right) \cdot 0.45 \quad (3)$$

The equation is based on the data obtained in Appendix C. Equations (4) and (5) are used to calculate the equivalent moving mass in horizontal and vertical directions for the complete hexapod.

$$m_{totH} = 4 \cdot m_{eqX} \cdot \left(\frac{\sqrt{3}-1}{2}\right) + 2 \cdot m_{eqY} + 4 \cdot m_{eqY} \cdot \left(\frac{-\sqrt{3}+3}{2}\right) + m_{End} \quad (4)$$

$$m_{totV} = 6 \cdot m_{eqZ} + m_{End} \quad (5)$$

Where m_{eq} is the equivalent mass of a single leg, evaluated at the top of the upper arm. The horizontal equivalent mass includes direct contributions from two legs and the end-effector, which each add their respective y-component of their moving mass, according to Figure 3. For the remaining four legs the direction of motion is rotated 120 degrees relative to their local coordinate frame, contributing a moving mass component in local x- and y-direction.

4.2 Results arc concept

The parameters for the arc concept, obtained by optimization, are presented in Table 4. Table 5 provides the simulated specifications using the optimal parameters, including the stiffness properties obtained in Appendix B and C and the stiffnesses of the designed base flexure presented in 4.4.

Parameter	Bounds	Optimum
L_1	0.2 - 0.5 [m]	477 [mm]
L_2	0.2 - 0.5 [m]	338 [mm]
θ_2	10 - 40 [deg]	30.1 [deg]
R	0.3 - 0.4 [m]	382 [mm]

Table 4: Optimal parameters of the arc concept

Parameter	Value
First eigenfrequency	
Rigid end-effector	126.0 [Hz]
Flexible end-effector	63.8 [Hz]
Horizontal eq. mass	2.36 [kg]
Vertical eq. mass	4.85 [kg]
Actuator stroke	18.0 [deg]
Maximum deformation	
Top universal joint	17.8 [deg]
Bottom universal joint	17.2 [deg]
Revolute joint	4.4 [deg]

Table 5: Simulated specifications of the arc concept, the given eigen frequencies are in combination with the 2.5 kg load case

The first eigenfrequency for the complete hexapod including flexible end-effector is calculated by taking the equivalent stiffness of the leg assemblies in series with the stiffness of the end-effector.

4.3 Results linear concept

In Table 6 the optimal parameters for the linear concept are presented. Utilizing these optimal parameters, the simulated specifications of Table 7 are obtained. The results of Tables 5 and 7 show that it is feasible for both concepts to meet the requirements on the mass and parasitic eigenfrequencies.

Parameter	Bounds		Optimum	
L_1	0.2-0.5	[m]	497	[mm]
L_2	0.2-0.5	[m]	230	[mm]
θ_2	40-90	[deg]	60.0	[deg]
R	0.345-0.4	[m]	381	[mm]

Table 6: Optimal parameters linear concept

Parameter	Value
First eigenfrequency	
Rigid end-effector	178.6 [Hz]
Flexible end-effector	68.4 [Hz]
Horizontal eq. mass	2.36 [kg]
Vertical eq. mass	4.79 [kg]
Actuator stroke	121 [mm]
Maximum deformation	
Top universal joint	16.1 [deg]
Bottom universal joint	16.1 [deg]
Revolute joint	4.4 [deg]

Table 7: Simulated specifications of the linear concept, the given eigen frequencies are in combination with the 2.5 kg load case

4.4 Base flexure

This subsection presents the revolute base flexure for the arc design, including an optimization to obtain the optimal design parameters.

The required stroke of the base flexure for the arc concept is about 20 degrees. No exceptional requirements on parasitic motion are applicable since, in contrast to an iron-core actuator, no negative stiffness is introduced. A cross flexure is an adequate choice due to its simple and economical design. In Figure 9 the cross hinge is presented, including its parametrization.

The base flexure is optimized for the highest first parasitic eigenfrequency of the hexapod. This is accomplished by defining the cost function as one

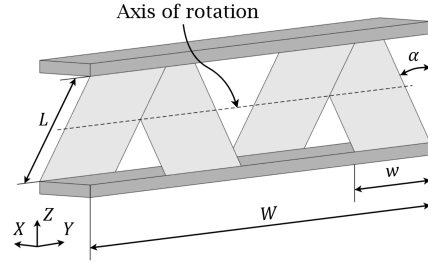


Figure 9: Parametrization of the base flexure

over the eigen frequency of the leg, with the stiffness's of the base flexure in series with the arm stiffness's according to Appendix B. In this manner, the best ratio between the support stiffness in the direction tangential to the motion and perpendicular to the motion is obtained. The axis of rotation is aligned to the center of the leaf springs, as this results in the lowest stress, which is a limiting factor in the optimization for the support stiffness. The stress is limited to 550 Mpa. The total width W of the base flexure is set to 100 mm, since this is about the width of the lower arm.

The optimization parameters along with their optimum are presented in Table 8, where w is the width of the individual leaf springs and t the thickness. Table 9 presents the simulated specifications of the base flexure utilizing the optimum parameters. The support stiffness of the base flexure in the translational x-direction is approximately an order of magnitude higher than the stiffness of the lower arm. Consequently, the base flexure is not the dominant factor for the first parasitic eigenfrequency.

Parameter	Bounds		Optimum	
L	5-50	[mm]	9.0	[mm]
w	5-25	[mm]	20.1	[mm]
t	0.25-0.5	[mm]	0.25	[mm]
α	10-50	[deg]	29.9	[deg]

Table 8: Optimal parameters of the base flexure

Parameter	Value	
Support stiffness's		
X-translational	$1.05 \cdot 10^8$	[N/m]
Y-translational	$1.27 \cdot 10^8$	[N/m]
Z-translational	$3.14 \cdot 10^8$	[N/m]
X-rotational	$3.23 \cdot 10^5$	[Nm/rad]
Z-rotational	$1.08 \cdot 10^5$	[Nm/rad]
Actuation stiffness		
Y-rotational	2.41	[Nm/rad]
Parasitic z motion	0.026	[mm]
Maximum stress	550	[Mpa]
Maximum deflection	10.0	[deg]

Table 9: Simulated specifications of the base flexure

5 Final Design

This chapter presents the transition from conceptual designs to final test setup designs.

5.1 Arc design

An illustration of the detailed leg assembly based on the arc concept is shown in Figure 10. Figure 11 provides a cross section of the final arc design. The main dimensions are based on the optimal parameters outlined in Sections 4.2 and 4.4. The design fits inside a build volume of 415x200x315 mm.

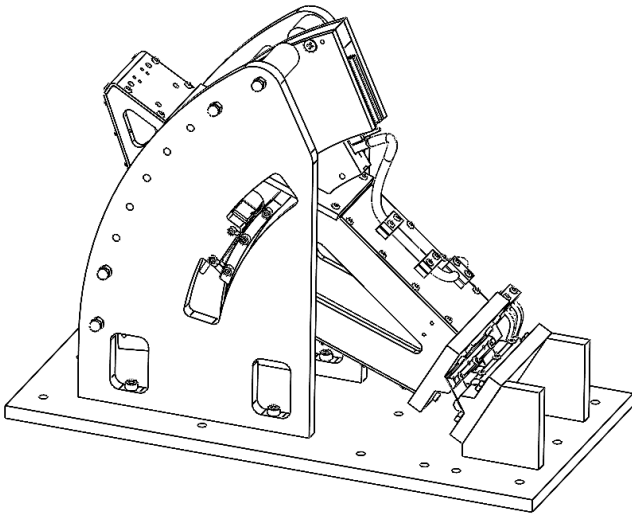


Figure 10: Final arc design

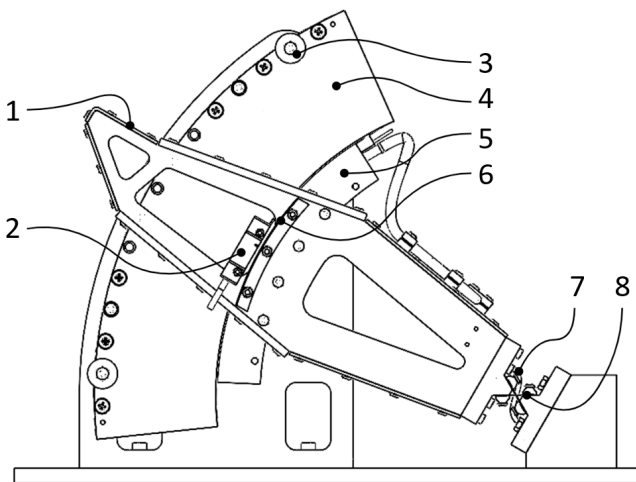


Figure 11: Cross section arc design, 1) Mounting surface universal joint 2) Encoder 3) Spacer 4) Actuator yoke 5) Actuator coil 6) Encoder strip 7) Cable flexure 8) Base flexure

The actuator coil (5) is mounted in the middle of the arm, to prevent the introduction of torsional effects. This implies that the actuator yoke (4) is positioned through the arm. The actuator yoke is clamped between two aluminum

plates with the use of spacers (3). The encoder (2) and encoder strip (6) are located as close to the actuation as physically feasible, to prevent non-collocation issues. The cost of this design is approximately €3,300. Including the motor drive and controller the total cost of the system is approximately €10,000.

5.1.1 Base flexure

The flexure elements are made from the stainless steel AISI 301 full hard, with a 1.185 MPa 0.2% proof stress and an endurance limit of 550 MPa [10]. The planar leaf springs are made from a single part, which is established by laser cutting, to improve alignment. The leaf springs are mounted using aluminum clamps provided with a notch to improve the clamping pressure, thereby reducing micro-slip.

5.1.2 Arm

The arm is manually designed and optimized for the highest stiffness with an inertia equivalent to the model used for the optimization in Section 4.2. The designed arm, including mounting materials, has a rotational inertia in the direction of motion of 0.0277 [kg m²], as obtained by CAD. Finite element software is used to obtain the stiffnesses, as described in Appendix B.

5.1.3 Cable routing

Typically, a cable slab results in significant hysteresis. The hysteresis finds its origin both in the material hysteresis and in geometrical nondeterministic behavior. With this hysteresis being a serious drawback, options are examined to minimize the effect. For the arc concept, a straightforward solution is to guide the cables through the center of rotation, to minimize the geometrical nondeterministic behavior, as illustrated in Figure 12. To address the material hysteresis, the cable is partially replaced with a wire flexure of the same material as the base flexure.

5.2 Linear design

Figure 13 presents the final linear design, in addition Figure 14 and 15 provide cross-sectional views to highlight the internal components.

The lower arm (6) is supported by eight air bearings from the manufacturer New Way Air Bearings. The square tube used in the optimization does not have common dimensions. The air bearings require a running surface with a minimum local flatness of half the air gap, which is about 3

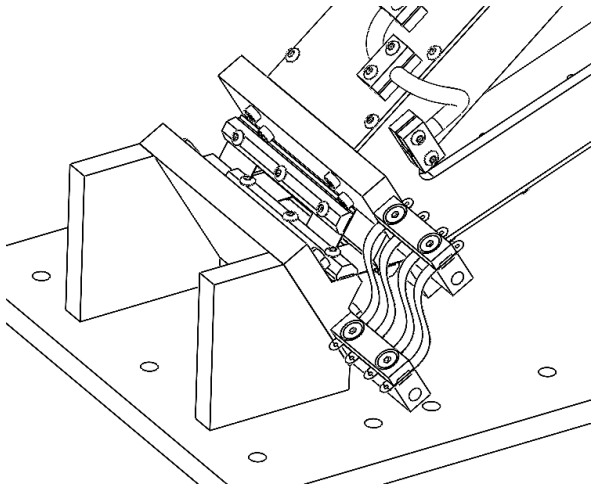


Figure 12: Cable routing arc setup

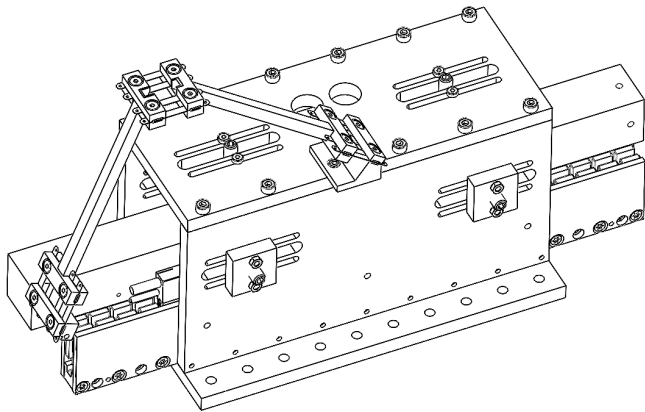


Figure 13: Final linear design

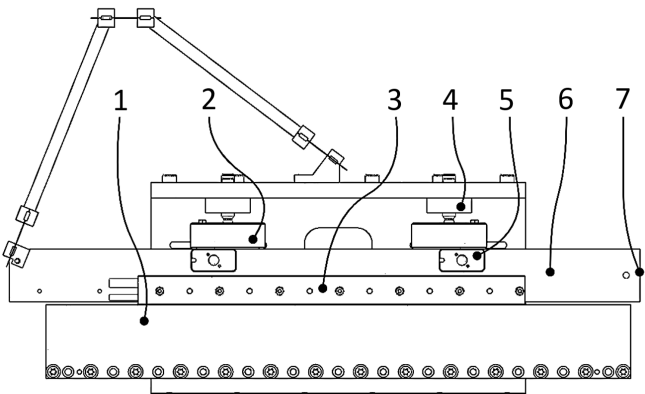


Figure 14: Cross section Linear design. 1) Actuator yoke 2) 25x50 mm air bearing 3) Actuator coil 4) Mounting block air bearing 5) 15x30 mm air bearing 6) Lower arm 7) Mounting surface universal joint

μm . Since the load of the air bearings cause deformations, the wall thickness has to be relatively large in proportion to the section width resulting in uncommon dimensions. The 35x35x4 mm tubing used in the optimization is primarily used for proof of concept and likely to be changed, if implemented in the complete final hexapod. Since the moving mass is not as important for the test setup,

a readily available solid square bar is used instead.

For the support in the x-direction four New Way Air Bearings S122501 (2) with dimensions 25x50 mm are used. The support in the y-direction is provided by the smaller S121501 with the dimensions of 15x30 mm, leaving space for mounting the actuator coil (3) and encoder (9).

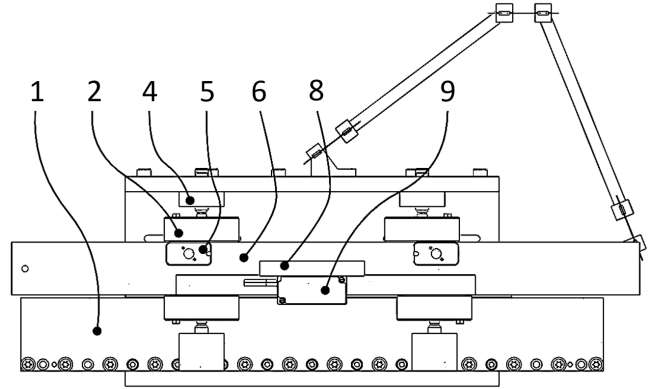


Figure 15: Cross section Linear design. 1) Actuator yoke 2) 25x50 mm air bearing 4) Mounting block air bearing 5) 15x30 mm air bearing 6) Lower arm 8) Encoder strip 9) Encoder

The test setup is designed to be adjustable in the position of the air bearings, to provide greater flexibility for future experiments. Similarly, the lower arm (6) is longer than obtained by optimization. The adjustability requires the air bearings to be mounted to additional mounting blocks (4).

The main dimensions of the linear design are 420x150x140 mm without the cable guide. In addition to the design presented in Figure 13, an extrusion profile frame is added to provide an end stop and additional mounting options. This results in the final dimensions of 675x160x260 mm, including the cable guide. Note that the design can be significantly reduced in size if the arm length is shortened.

The cost of this design is approximately €6,500, making the linear design a less cost-effective option compared to the arc design. Including the motor drive and controller, the total cost of the system is approximately €13,200.

5.2.1 Cable guide

A two-linkage cable guide is designed to reduce the hysteresis effects of the power cable. Identical to the arc design, laser cut AISI 301 full hard flexures are used as the cable cores. It is of high importance that the cable guide has a sufficiently high first parasitic eigenfrequency. Therefore, a modal analysis is performed in SPACAR, which indicates a minimum first parasitic eigenfrequency of 86.3

Hz over its range of motion. The cable guide constrains the rotation in the direction of motion of the lower arm. This rotation is not constraint by the air bearings, such that no overconstraints are introduced by the cable guide. For further details, refer to Appendix D.

As demonstrated in Section 6.1, insulation significantly increases the hysteresis. Consequently, insulation is solely applied at the clamping contacts in conjunction with protective covers to prevent short circuits.

5.3 Controller design

The validation of the concepts requires position controllers to track a position reference. The tracking performance does not directly influence the hysteresis measurements. The error in the hysteresis tests is only dependent on the measurements on the reaction forces associated to positions, meaning that precise tracking is not critical for validation. For the position control, a PID controller is used. The position controller has a reference current as an output, which is the input for the built-in current control loop of the AccurEt 48 motor driver by ETEL. As a design choice for the controller, the crossover frequency is aimed to match the desired crossover frequency for the complete hexapod, which is 10 Hz.

6 Validation

The performance validation includes hysteresis tests of the test setups. Prior to these tests, a prototype of the cable guide for the linear design is evaluated to assess the hysteresis introduced by the moving power cable. Additionally, system identification is performed to characterize the dynamic behavior of the test setups.

6.1 Test prototype cable guide

An individual test setup is developed for the moving cable of the linear design to obtain information about the introduced hysteresis. First, a baseline measurement is performed with a 4G 0.75 mm² cable, similar to the power cable of the linear actuator. The cable is spanned between the fixed world and a carriage, demonstrating the hysteresis effect without any cable routing solution. Subsequently, a cable guide with aluminum links and 3D-printed clamps is evaluated, both with and without insulated flexures, as presented in Figure 16. The cable guide is moved to predefined positions while the position and reaction force of the carriage connected to the cable guide are measured. For both

tests, at the center of the range of motion (reference position), the distance between the connection to the fixed world and the connection to the carriage is 250 mm.

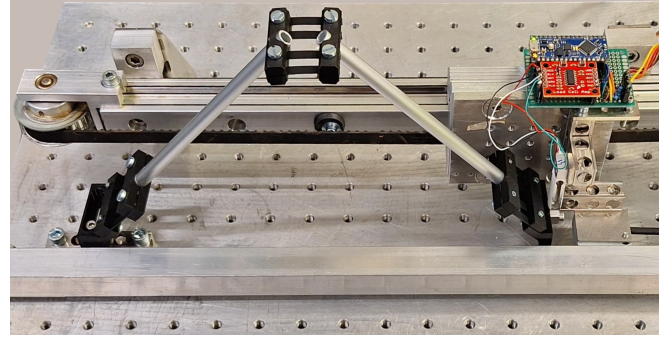


Figure 16: Test setup prototype cable guide (with heat shrink insulated flexures)

Figure 17 presents the hysteresis curve of the baseline test on solely the cable. The data is only plotted at discrete positions, since the carriage is stopped at these positions to eliminate forces resulting from accelerations. The data points are stacked vertically due to a reduction in force over time as a result of creep. The interpolated hysteresis loop forms a connection, this differs from the actual path that is made during the test. In Figure 18 the same test is performed on the cable guide, without insulated flexures. To validate the test results, the SPACAR model from Appendix D is used to plot the simulated reaction force.

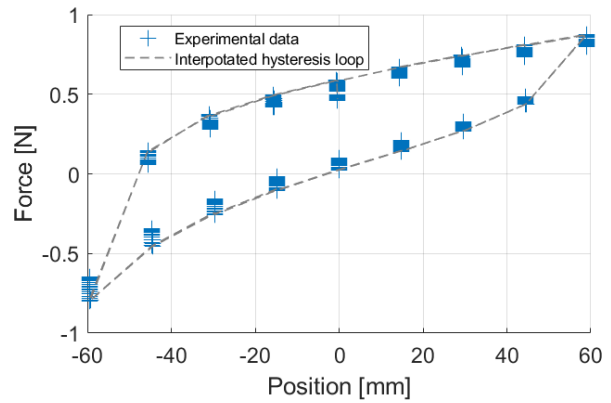


Figure 17: Hysteresis curve 4G 0.75 mm² cable, with a length of 450 mm to ensure a light bend in the cable during its whole range of motion

Hysteresis is defined as the difference in reaction force at the same position due to the previous state. To determine the hysteresis force, the carriage is displaced with half the actuator stroke in either direction, refer to Figure 19. In the graph, the creep in the cable is clearly visible. The hysteresis force for the 4G 0.75 mm² cable is 0.66 N. For the cable guide, the hysteresis force is 0.0035 N, about 99.5%

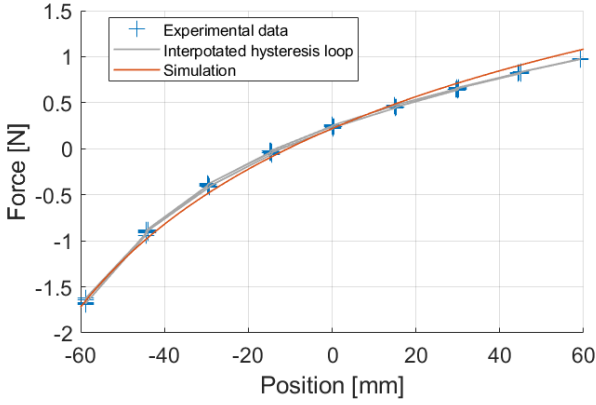


Figure 18: Hysteresis curve cable guide

lower than that of the 4G 0.75 mm² cable. The same experiment is also performed in combination with fully insulated flexures. Kapton tape insulation increases the hysteresis force to 0.045 N, while heat shrink results in an increase to 0.053 N.

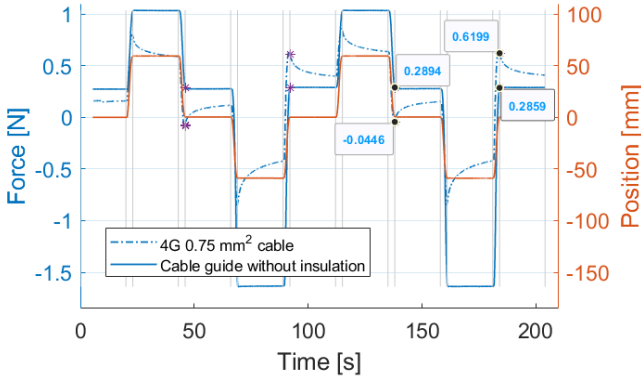


Figure 19: Hysteresis 4G 0.75 mm² cable and cable guide

6.2 System identification

System identification ensures that the systems exhibit the expected dynamic behavior and provides insights into system parameters and potential parasitic eigenfrequencies. A chirp reference is sent to the actuators in an open loop, to obtain the input-output relation, as presented in Figures 20 and 21.

The measured response is fitted with a single-degree-of-freedom model representation. The fitted parameters are listed in Table 10. For the arc setup, the deviation from the inertia obtained by CAD corresponds to 30 g at the interface to the universal joint. For the linear setup, the mass deviates 50 g. Additionally, the motor constants are calibrated to ensure a valid current-to-force relation.

The phase drop at higher frequencies observed in both systems can be attributed to delays in the drive. During validation, the drive operated on a 1 kHz sampling frequency.

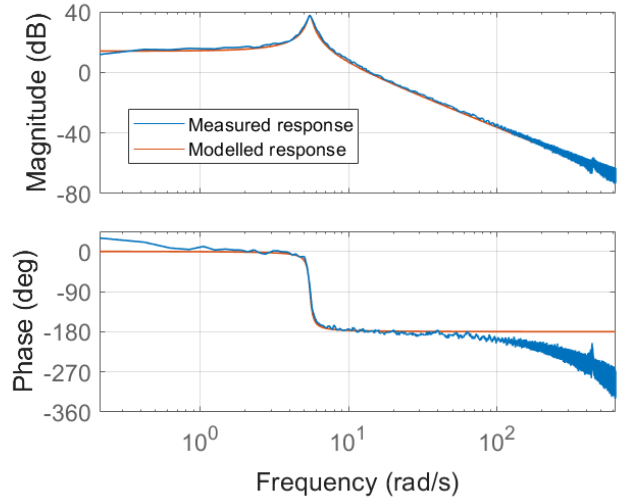


Figure 20: System identification arc setup

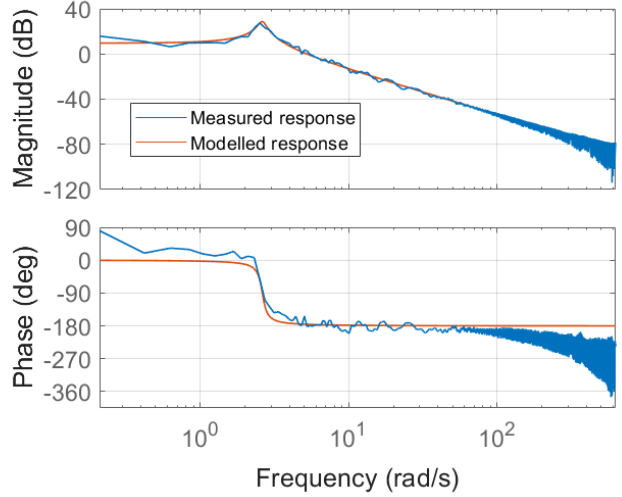


Figure 21: System identification linear setup

Parameter	Value	
I_{arc}	0.076	[kg/m ²]
k_{arc}	2.4	[Nm/rad]
d_{arc}	0.03	[Nm·s/rad]
m_{lin}	1.76	[kg]
k_{lin}	12.0	[N/m]
d_{lin}	0.05	[N·s/m]

Table 10: Identified parameters

6.3 Validation arc design

Figure 22 shows a photograph of the test setup used to obtain the data presented in this subsection. Additional pictures of the test setups can be found in Appendix E.

Hysteresis measurements serve as a key performance indicator for the hexapod leg designs. Hysteresis refers to the difference in force at the same position due to the system's previous state. The force is directly related to the motor current; this



Figure 22: Photograph of the arc design test setup

relationship is utilized in the tests. To evaluate hysteresis, the arm is excited with a sine wave of 0.03 Hz, while position and current are measured. The position is measured by the system's encoder. The frequency is sufficiently low to ensure acceleration effects can be neglected.

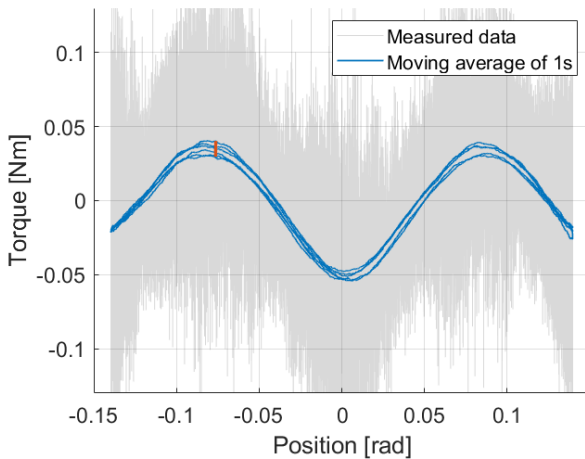


Figure 23: Actuator torque plotted against angle, compensated for flexure stiffness

In Figure 23 the results of the hysteresis test are shown, in which three complete periods are performed. The output current of the motor drive consists of a significant amount of noise. This noise consists of sensor error and the actual error between the reference current and the real current output. The sensor noise directly translates to an error on the hysteresis measurement. This is not the case for the actual error on the real current output. However, the relatively high-frequency fluctuations of the current result in the system no longer being quasi-static, thereby introducing error into the hysteresis measurement. To exclude drive-related effects, a moving average of 1 s is used to only filter out the high-frequency behavior, which reveals a maximum hysteresis of 0.0083 Nm.

In Figure 23, fluctuations in torque can be observed, known as torque ripple. The period of the torque ripple seems to consist of harmonics rela-

tively close to the magnet pitch of the actuator. The magnet pitch (N-N) of the IL91C is 0.157 radians [6]. Furthermore, the torque ripple is very repeatable.

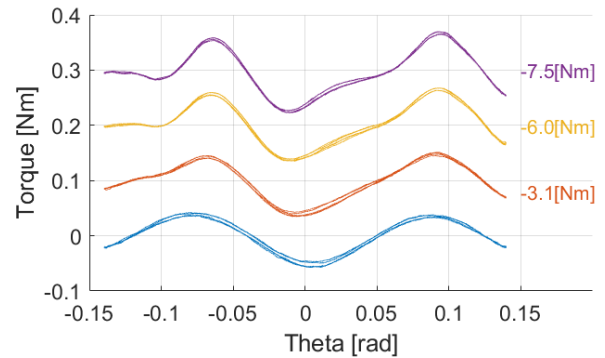


Figure 24: Actuator torque plotted against angle including force dependency, compensated for stiffness and including offsets

Figure 24 shows the force dependency of the torque ripple. In this figure, an identical hysteresis experiment as presented in Figure 23 is plotted under different loads. To visualize the torque ripple for the higher loads, the data is corrected for stiffness and offset.

To validate whether the hysteresis at the encoder is representative to the hysteresis at the mounting surface of the universal joint, an additional test with a capacitive sensor (Lion Precision C8) is performed. The hysteresis loop provided in Figure 23 is evaluated at the encoder indicated with (2) in Figure 11. Ideally, the hysteresis would be evaluated at the mounting surface of the universal joint, indicated with number (1) in figure 11, since this hysteresis will transfer to the end-effector. Hysteresis effects in the base flexure may induce a rotational displacement that remains undetected if the rotation axis coincides with the encoder. For instance, a pivot shift at the base flexure caused by hysteresis could lead to greater hysteresis at the mounting location of the universal joint than what is observed at the encoder.

In this test, a multi-step reference is used to position the arm to the middle and ends of the range of motion. After completing one full loop, while the arm is in the middle of the range of motion, the capacitive sensor is positioned to measure the distance to the end of the arm, indicated with (1) in Figure 11. Whereafter, the arm is moved to the end of the range of motion and back. Since the capacitive sensor gives a relative position, the differences between the two measurements are compared to the difference in position measured at the encoder. Figure 25 presents the data obtained by this test procedure, where the capacitive sensor data is off-

set to match the absolute encoder at the time instance 130-150 s.

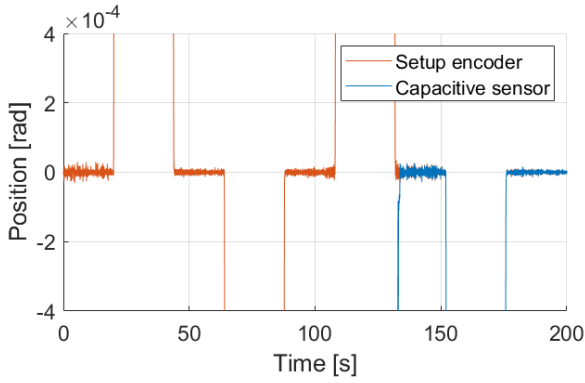


Figure 25: Encoder and capacitive sensor readout over time during hysteresis validation, with the raw capacitive sensor data offset to match the relative position of the capacitive sensor to the absolute encoder at the time instance 130-150 s

Figure 26 provides the data of Figure 25 on a narrow time window. The fluctuations observed in the setup's encoder data are also present in the capacitive sensor data. However, the capacitive sensor data appeared to consist of additional noise. Therefore, the capacitive sensor data is filtered by a moving average of 0.01 seconds. A difference in

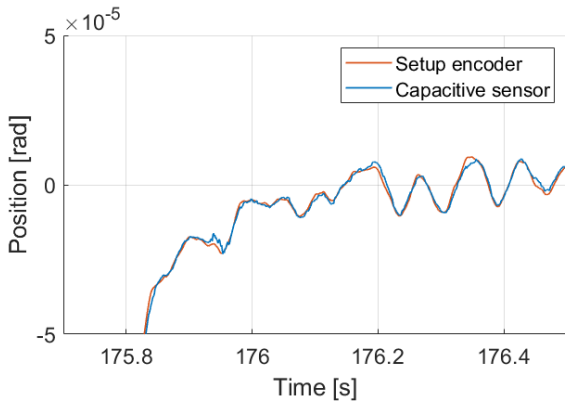


Figure 26: Detailed view of encoder and capacitive sensor readout over time, during hysteresis validation

hysteresis would be related to the position difference between the two time intervals: 130-150 s and 180-200 s. The position difference is evaluated both for the system's encoder as well as the capacitive sensor. The difference between these two measurements indicate whether the hysteresis measured at the encoder is representative to the hysteresis at the mounting location of the universal joint. The difference between the encoder and the capacitive sensor is measured to be about 185 nrad, which corresponds to 60 nm at the mounting surface of the universal joint. To exclude the high-frequent

fluctuations in the data, averages on a 0.5 s window are used to calculate this difference between the encoder and the capacitive sensor.

6.4 Validation linear design

Figure 27 shows a photograph of the test setup used to obtain the data presented in this subsection. For additional pictures of the test setups, see Appendix E. The hysteresis of the linear design is



Figure 27: Photograph of the linear design test setup

evaluated in a similar manner as described in Section 6.3. The arm is excited with a sine wave of 0.03 Hz, while position is measured with the encoder of the setup itself; the force is calculated utilizing the measured motor current.

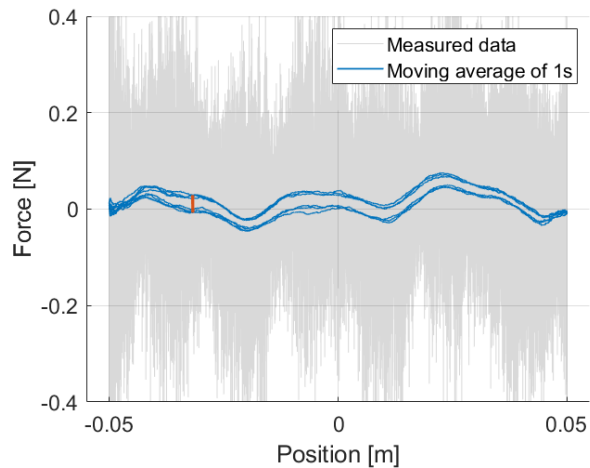


Figure 28: Actuator force plotted against position, compensated for flexure stiffness

Figure 28 provides three full periods of the hysteresis loop. Again, the data is corrected for stiffness and offset. The maximum measured hysteresis is 0.0371 N, indicated in orange. The torque ripple shows behavior similar to that of the arc motor. The period of the torque ripple closely matches the magnetic pitch of the UM12, which is 30 mm (N-N) [7]. Figure 29 shows the force dependency of the torque ripple.

When the data of Figure 29 is fitted with the fol-

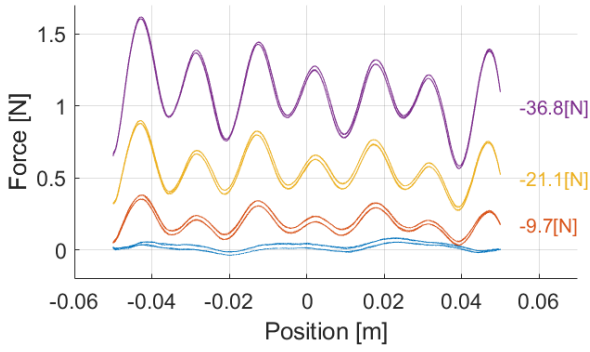


Figure 29: Actuator force plotted against position including force dependency, compensated for stiffness and including offsets

following equation:

$$f(x) = a_0 + a_1 \cdot \cos(x \cdot w) + b_1 \cdot \sin(x \cdot w) + \dots + a_8 \cdot \cos(8 \cdot x \cdot w) + b_8 \cdot \sin(8 \cdot x \cdot w) \quad (6)$$

a magnitude plot as Figure 30 can be created. In this figure it is evident that the torque ripple consists of two dominant frequencies, for which the amplitudes are force dependent.

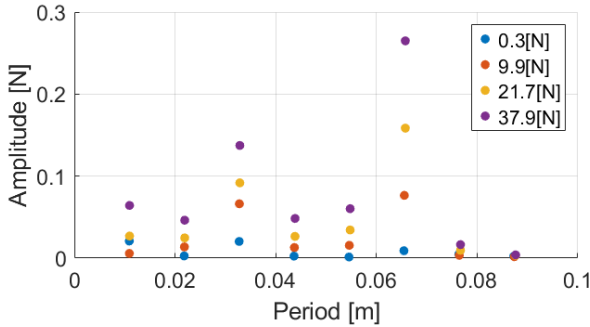


Figure 30: Force dependency of frequency content present in torque ripple linear setup

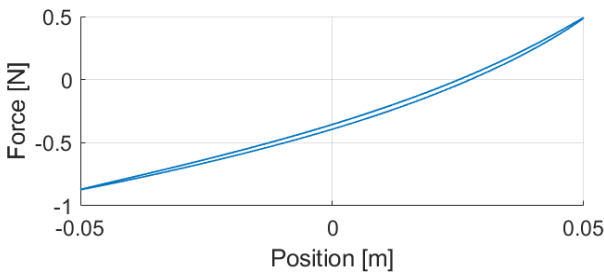


Figure 31: Cable guide reaction force plotted against position

The tests conducted on the prototype of the cable guide, provided in Section 6.1, show that the hysteresis with fully Kapton insulated flexures is larger than the total system hysteresis of the final linear setup. To evaluate the hysteresis contribution of the cable guide in the complete setup, a

similar test to the tests discussed in Section 6.1 is performed on the actual final cable guide.

The cable guide is on one side connected the lower arm and on the other side to the fixed frame, as shown in Figure 14 and 15. In the test, a load cell is mounted between the cable guide and the frame, to measure force parallel to the direction of motion of the lower arm. Figure 31 shows the resulting hysteresis loop. The maximum hysteresis is 0.03647 N.

7 Discussion

Hysteresis measurements serve as a key performance indicator for the hexapod leg designs. For the arc design, a maximum hysteresis of 0.0083 Nm is measured, which is 0.023% of the continuous torque. The hysteresis torque corresponds to a force of 0.025 N, at the mounting surface of the universal joint. The linear design showed a hysteresis of 0.037 N, equivalent to 0.032% of its continuous force. Thus, the arc design has 26.9% less hysteresis than the linear design.

For context, tests on the actuator assembly of the T-Flex showed a hysteresis of 0.15 Nm [11], with a continuous torque output of 21.9 Nm and an ultimate torque of 55.5 Nm [12], yielding a relative hysteresis of 0.68%. In comparison, the arc design not only reduces the relative hysteresis found in the T-Flex to 3.4%, but also increases the continuous torque to 35.6 Nm and the peak torque to 142 Nm [6]. The linear design reduces the relative hysteresis to 4.7% correspondingly.

Further analysis revealed that 98% of the hysteresis observed in the linear configuration originates from the cable guide. This emphasizes the necessity of optimizing the cable routing. In Section 6.1, the initial 3D-printed prototype of the cable guide was evaluated. It is important to note that the TAL221 load cell from HT Sensor Technology, used in these experiments has a hysteresis of 0.0025 N [13]. Without any insulation a hysteresis of 0.0035 N was found. Covering the complete flexures with Kapton tape increased the hysteresis significantly to 0.045 N.

By contrast, the final cable guide design, which incorporates Kapton isolation only at the clamping surfaces, yields a hysteresis of 0.0365 N. This indicates that the majority of the hysteresis introduced by the Kapton in the initial test originated from the clamping interface. These results suggest that directly clamping the flexures with a plastic interface yields lower hysteresis than using aluminum clamping elements in combination with Kapton isolation. Additionally, the results suggest that the

overall hysteresis of the linear design could be significantly reduced.

The maximum applied force in the hysteresis tests is approximately one-fourth of the continuous torque and force ratings. As a result, thermal effects—such as the heat generation in the actuator or cable guide—are not fully represented in the experimental conditions. However, repeated operation at this load level did not exhibit any appreciable variation in performance.

The validation of the hysteresis measurements on the arc setup using the capacitive sensor shows a difference of 60 nm at the mounting surface of the universal joint, between the setup encoder and the capacitive sensor. The measured difference is close to the sensor’s repeatability limit, and may not be fully distinguishable from sensor error. Consequently, no significant variation between the setup’s encoder and capacitive sensor is found for this quasi-static case.

In Figure 25, the data may give the impression that a significant amount of noise is present. However, a closer look at Figure 26 shows that it is actually the system which is moving. This steady-state error can be explained by noise on the output current of the drive. The absence of friction makes the system highly sensitive to variations in applied forces, which was also observed in [4].

The capacitive sensor appears to suffer from significantly more noise than the encoder. This could be explained by the limited performance of the Texas Instrument LAUNCHXL-F28379D LaunchPad, which was used for the analog reading of the capacitive sensor.

Instability of the air bearings was observed in the case the linear design reached the limits of its range of motion. The spacing between the air bearings is designed to be adjustable for experimental flexibility which required the length arm to be longer. This created a relatively large overhang at full extension. In this configuration, even small excitations perpendicular to the direction of motion were amplified rather than damped out. Nonetheless, this effect was not observed during testing.

Adjustment of the preload on the air bearings proved to be a challenging and tedious task due to the high adjustment sensitivity and the lack of a robust locking mechanism. As a result, repeated fine-tuning was required during testing. This issue could likely be mitigated by implementing larger air bearings and finer pitch set screws with a robust locking mechanism, for better control and robustness. In contrast, the arc design is significantly easier to assemble and operate, and proved to be more robust than the linear design.

Torque ripple was observed in both test setups.

In general, torque ripple can have a variety of origins. In this case, it does not originate from a cogging effect, since ironless-core motors do not suffer from a magnetic attraction between the stator and coil when unpowered, as discussed in Section 3.1. It is also not likely to be a back-EMF distortion, since the effect is not velocity dependent. The ripple showed harmonics near the magnet pitch, potentially linked to variations in the motor constant as a result of imperfect commutation by the drive.

The torque ripple is highly repeatable, which facilitates effective correction. Another option for minimizing the torque ripple could possibly be found in adopting a non-commutating actuator, for example a voice coil with an increased stroke of Physik Instrumente, briefly mentioned in Appendix A.

Finally, as discussed in Section 4, the optimization parameters are based on preliminary design choices on a single leg model. For optimal performance, however, optimization should be based on a model of the full hexapod, incorporating the design of the upper arms and end-effector. While this is unlikely to significantly change the test results, it could improve the overall specifications of the hexapod.

8 Conclusion

This paper presents and evaluates two potential leg solutions for a low hysteresis large-range-of-motion hexapod developed for a hybrid testing application. The explored architectures include an arc design with a 6-RURU kinematic structure including flexure elements, and a linear design utilizing air bearings, in a 6-PURU configuration.

The proposed innovative solution for minimizing hysteresis caused by a moving power cable makes a moving-coil configuration suitable for low-hysteresis actuation. This enables the option to utilize ironless core actuators while still meeting the tight requirements for moving mass, actuation forces, and hysteresis. The ironless core actuators suffer significantly less from torque ripple and hysteresis resulting in a lower overall hysteresis and a cogging-free system.

The validation shows a maximum hysteresis of 0.0083 Nm for the arc design, which is 0.0233% of its maximum continuous torque. For the linear setup, a hysteresis of 0.037 N is measured, which corresponds to 0.0319% of the continuous force. This study contributes to the ongoing development of precision hexapods by reducing hysteresis to 3.4% and 4.7% in the arc and linear design respectively, compared to the T-Flex reference.

The performance limitations due to hysteresis are effectively eliminated, as the hysteresis will no longer be the critical factor in the current designs. For improving positioning, minimizing the current noise will be of the primary interest. Additionally, effective correction of the torque ripple will be necessary to improve the estimation of end-effector loads based on the measured motor current.

Among the two concepts, the arc configuration is identified as the most suitable candidate for the hybrid testing application. First, the arc design is easier to assemble and operate, and more robust than the linear design. Second, the arc design is more cost effective than the linear design. Third, the arc design has 26.9% less hysteresis than the linear design. Fourth, the arc design offers greater design flexibility, as the equivalent mass and actuation force at the mounting surface of the universal joint can be adjusted by varying the length of the lower arm. The proposed hexapod design directly contributes to the development of hybrid testing applications of floating wind turbines, enhancing the acceleration of offshore renewable energy innovations.

Future work will focus on the modeling and optimization of the complete hexapod, including the design of the upper arms and end-effector. Furthermore, a more detailed study on the torque ripple is required for effective correction. In this manner, a hexapod with improved hysteresis and high precision performance can be created. This will further expand the capabilities of precision hexapods, which could enhance the applications of precision hexapods even further.

References

- [1] X. Sun, D. Huang, and G. Wu. "The current state of offshore wind energy technology development". In: *Energy* 41.1 (2012), pp. 298–312. ISSN: 0360-5442. DOI: <https://doi.org/10.1016/j.energy.2012.02.054>.
- [2] I. Bayati, A. Facchinetti, A. Fontanella, H. Giberti, and M. Belloli. "A wind tunnel/HIL setup for integrated tests of Floating Offshore Wind Turbines". In: *Journal of Physics: Conference Series* 1037 (June 2018). DOI: 10.1088/1742-6596/1037/5/052025.
- [3] Hybrid labs. *HybridLabs - Accelerating Dutch innovations in offshore renewables through data-driven hybrid labs*. Accessed: 2025-01-06. 2025. URL: <https://hybridlabs.tudelft.nl/> (visited on 06/01/2025).
- [4] M. Naves, M. Nijenhuis, W.B.J. Hakvoort, and D.M. Brouwer. "Flexure-based 60 degrees stroke actuator suspension for a high torque iron core motor". In: *Precision Engineering* 63 (2020), pp. 105–114. ISSN: 0141-6359. DOI: <https://doi.org/10.1016/j.precisioneng.2020.02.001>. URL: <https://www.sciencedirect.com/science/article/pii/S0141635919308104>.
- [5] M. Naves, M. Nijenhuis, B. Seinhorst, and W.B.J. Hakvoort and. "T-Flex: A fully flexure-based large range of motion precision hexapod". In: *Precision Engineering* 72 (2021), pp. 912–928. ISSN: 0141-6359. DOI: <https://doi.org/10.1016/j.precisioneng.2021.08.015>.
- [6] Suzhou ITG Linear Motor Co. *IL91C Series*. Accessed: 2025-06-06. 2023. URL: https://en.itg-motor.com/products/ironless_linear_motors/50.html (visited on 06/06/2025).
- [7] Tecnotion. *Ironless linear motor series*. Accessed: 2025-06-06. 2024. URL: https://www.tecnotion.com/wp-content/uploads/2024/11/Brochure_Ironless_English_v1-1.pdf (visited on 06/06/2025).
- [8] K.S. Dwarshuis and M. Nijenhuis. "Five universal flexure joints for large range of motion, optimized for vertical support". To be submitted to Precision Engineering.
- [9] M. Naves, R.G.K.M. Aarts, and D.M. Brouwer. "Large stroke three degree-of-freedom spherical flexure joint". In: *Design and optimization of large stroke flexure mechanisms*. 2017.
- [10] Salomon's Metalen bv. *acceptance test certificate*. May 2019.
- [11] B. Seinhorst and W.B.J. Hakvoort. "Efficient formulation of hexapod kinematics enabling real time adaptive feedforward control". In: *2021 IEEE/ASME International Conference on Advanced Intelligent Mechatronics, AIM 2021*. IEEE/ASME International Conference on Advanced Intelligent Mechatronics (AIM). IEEE, Aug. 2021, pp. 186–191. ISBN: 978-1-6654-4140-7. DOI: 10.1109/AIM46487.2021.9517402.
- [12] Tecnotion. *Frameless torque motor series*. Accessed: 2025-06-06. 2024. URL: https://www.tecnotion.com/wp-content/uploads/2024/11/Brochure_Frameless_Torque_2.3.pdf (visited on 06/06/2025).

- [13] TAL221 MINIATURE LOAD CELL. *IL91C Series*. Accessed: 2025-06-06. URL: <http://www.htc-sensor.com/products/140.html> (visited on 06/06/2025).
- [14] Jeffrey Uitbeijerse. "T-Flex ELC: Aflexure-based hexapod with economic actuation, sensing and kinematics". In: 38 (2024).

A Supplementary Notes on Conceptual Designs

A rotational design incorporating air bearings, as well as an alternative linear configuration, were eliminated during the conceptual design phase. Appendix A provides a more detailed discussion of these concepts and the underlying considerations.

A third concept—combining an ironless torque motor with air bushings—was eliminated during the evaluation process. This decision was based on two main reasons. First, the LSI 224-67 torque motor from Maccon—initially intended for use—had a price tag about ten times higher than the actuators of the other concepts. Second, the selected air bearing supplier indicated that air bushings were unsuitable for the application. The issue would arise because of the dynamic loading of the air bushings in combination with the required preload. Unlike flat air bearings, the preload in air bushings cannot be adjusted, since their air gap depends on the tolerance between the bushing and the shaft. Given the dynamic loading conditions in the application—where forces may act in all directions—the shaft would move through the point of perfect concentricity with the bushing. As a result, the shaft would coincide with the lowest support stiffness and lack sufficient preload. The air bearing supplier stated the air bushings were unsuitable for the intended use.

However, a subsequent consultation with a different air bearing supplier indicated that the dynamic loading in combination with air bushings does not pose any concerns. The supplier suggested that off-the-shelf solutions could be modified to meet the application's requirements, indicating that a rotational concept incorporating air bushings may still hold potential. Specifically, utilizing the ironless torque motor a rotational design could be created without moving coils.

Other concepts such as an ironless tubular shaft motor in combination with air bushings, were also considered. The tubular shaft motor produces a linear motion while the rotation of the magnetic shaft is unconstrained. Two air bushings could guide the shaft, constraining its motion in radial directions while permitting both axial translation and rotation. This eliminates the need for an additional revolute joint in the upper arm and requires only two air bushings. However, this concept could not satisfy the mass constraints and was therefore eliminated.

Voice coil actuators may offer opportunities for the kinematic structure, as demonstrated in [14], presenting a commutation-free, elegant, and eco-

nomical design. Physik Instrumente is currently in the process of developing a voice coil motor specifically for this application. Preliminary results indicate that it is likely feasible to achieve a sufficient increase in stroke. Potentially enabling voice coil motors to satisfy the requirements. Voice coil actuators could pose opportunities for the kinematic structure, as demonstrated in [14], presenting a commutation free, elegant, and economical design.

B Finite Element Analysis Arm

Appendix B provides the horizontal, vertical and torsional stiffness's for the lower arm of the arc design.

To evaluate the dynamic performance of the system, individual stiffnesses are analyzed. The arm assembly is modeled in the FEM software of Solid-Works. A static analysis with unit loads is used to evaluate the stiffness properties of the arm.

The sheet metal is modeled with the parabolic triangular shell elements. At the connection with the actuator, the displacement u_z is constraint. At edge of the base, all translations are constraint, as a result also the angular displacements r_z and r_x are constraint.

In figures 32 to 35 the results of the FEM analysis are shown.

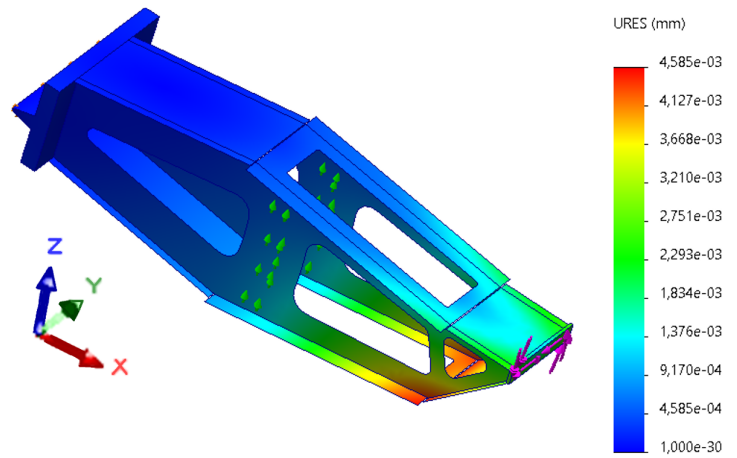


Figure 34: Resultant deflection under torsional unit load in x-direction

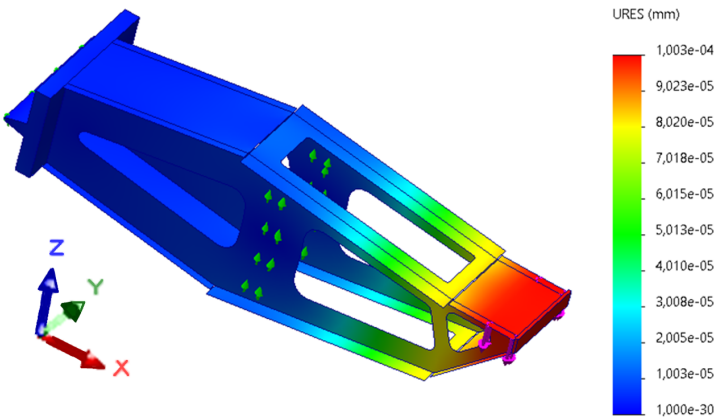


Figure 32: Resultant deflection under vertical unit load

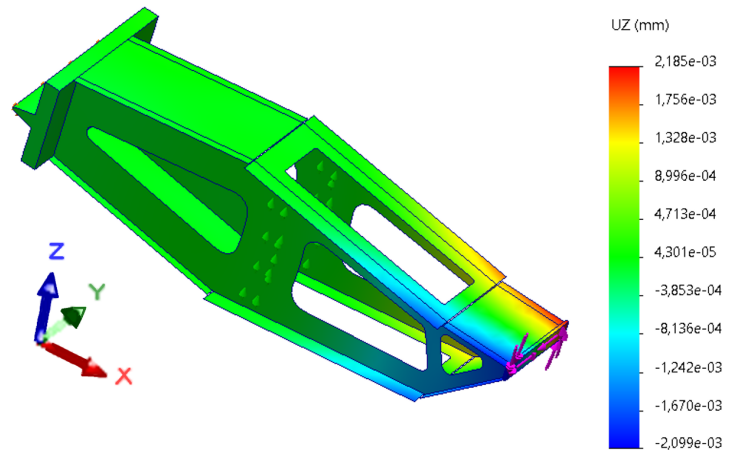


Figure 35: Y-deflection under torsional unit load in x-direction

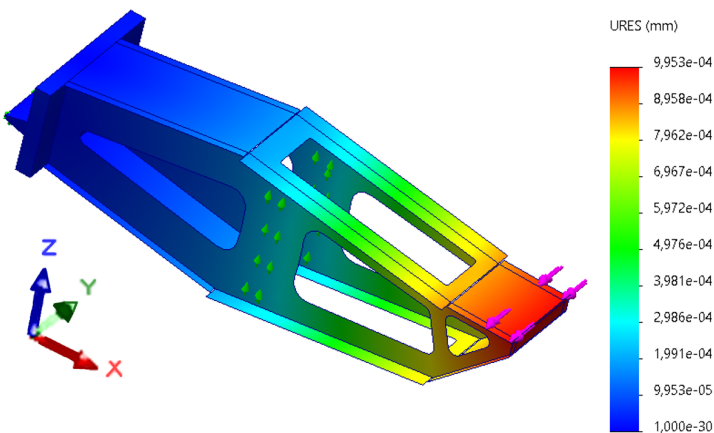


Figure 33: Resultant deflection under horizontal unit load

In Table 11 the calculated stiffnesses are presented.

Parameter	Value
Vertical stiffness	$1.0 \cdot 10^7$ [N/m]
Horizontal stiffness	$1.0 \cdot 10^6$ [N/m]
Torsional stiffness	$1.4 \cdot 10^4$ [Nm/rad]

Table 11: Stiffness's of the lower arm

C Finite Element Analysis End-Effector

Appendix C provides a modal analysis and mass properties for a conceptual end-effector design performed in ANSYS.

The end-effector significantly contributes to the equivalent mass and compliance of the hexapod. To ensure a valid leg optimization and conversion of the leg performance to the hexapod requirements, realistic end-effector properties are essential. Although the design of the end-effector is beyond the scope of this research, a conceptual design is proposed to estimate the required end-effector properties. Manual topology design optimization for the first parasitic eigenfrequency showed the most promising results for a star-like end-effector design, as illustrated in Figure 36. The simulation software of ANSYS is used to perform modal analysis on the design. In the modal analysis the connections to the hexapod legs are considered fixed in all translational directions. The 2.5 kg load is included in the analysis, and rigidly connected to the center tube at a vertical height of 1 m. For the material, general carbon sheets are used as a stiff and lightweight structure is required.

As expected, the first eigenfrequency corresponds to the swinging motion of the applied load about the center of the end-effector, as shown in Figure 36.

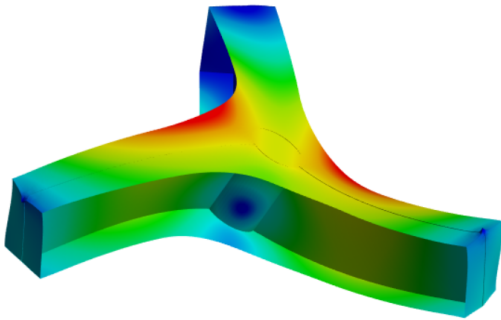


Figure 36: Mode shape of the first eigenfrequency for the end-effector with a radius of 400 mm

Radius R [mm]	Frequency [Hz]	Mass [kg]
200	79.1	0.433
250	80.1	0.488
300	79.0	0.566
400	73.2	0.744
500	68.3	0.877
600	63.4	1.032

Table 12: First eigenfrequencies and mass properties derived from ANSYS

In Table 12 the results of the modal analysis are

presented. Figure 37 shows a drop in the first eigenfrequency for small end-effector radii. This trend can be explained by observing the mode shapes. For small radii, shear stiffness is dominant, as visible in Figure 38. Since shear stiffness is proportional to the radius, decreasing the eigenfrequency for small radii. For larger radii the bending stiffness becomes dominant, according to the results this is approximately a linear relation. This indicates that the stiffness is quadratically inversely proportional to the end-effector radius, this behavior is in line with the Euler–Bernoulli beam theory, assuming the end-effector is modeled as three beam elements.

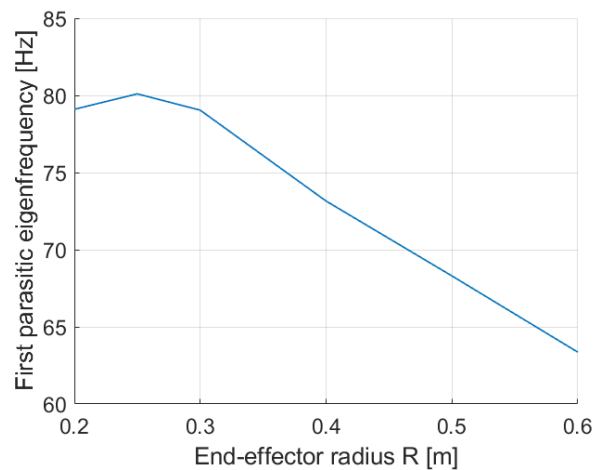


Figure 37: First eigenfrequencies as a function of the end-effector radius

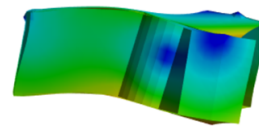


Figure 38: First mode shape for R = 200 mm

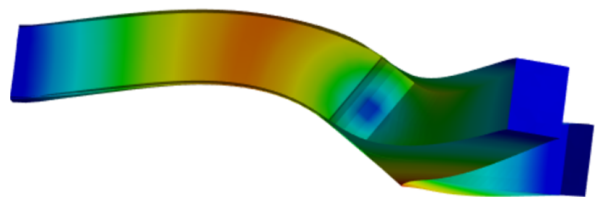


Figure 39: First mode shape for R = 600 mm

D Modal Analysis Cable Guide

Appendix D provides a modal analysis on the cable guide, performed in SPACAR.

The cable guide introduces additional eigenmodes to the system. For the performance of the hexapod, it is essential that the associated eigenfrequencies exceed the specified threshold of 50 Hz. This threshold is necessary to ensure stability while meeting the required control bandwidth. To evaluate the eigenfrequencies and validate the test results with the reaction forces, a SPACAR model of the cable guide is created, as shown in Figure 40

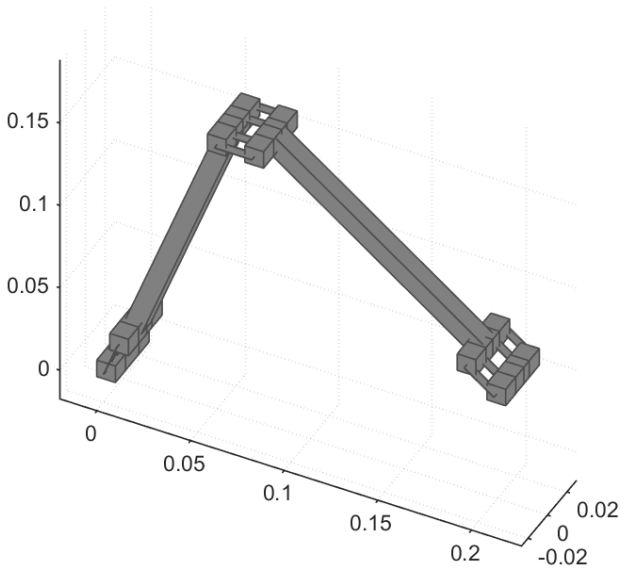


Figure 40: SPACAR model of the cable guide

Each set of flexure elements can be considered as a single leaf spring, introducing three constraints. In total, there are nine constraints and 6 DOFs, due to the two intermediate bodies, and since both ends of the cable guide are fixed. In the top of the cable guide, where the two linkages are connected, the out-of-plane translation is overconstrained. As a result, the cable guide has four internal parasitic eigenfrequencies due to underconstraints, the corresponding mode shapes are presented in Figures 41 to 44.

The eigenfrequencies of the cable guide are dependent on its configuration. Figure 45 shows the relation between the first parasitic eigen frequency and the position of the cable guide. At the limit of the range of motion, the lowest parasitic eigenfrequency is 86.3 Hz, which is well above the required 50 Hz.

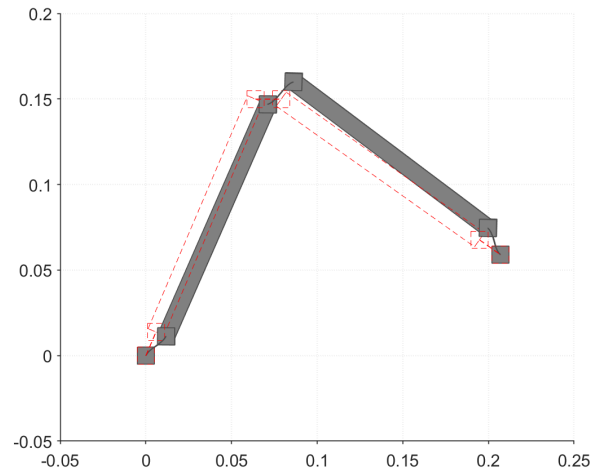


Figure 41: Mode shape 1 at 110.2 Hz in reference position

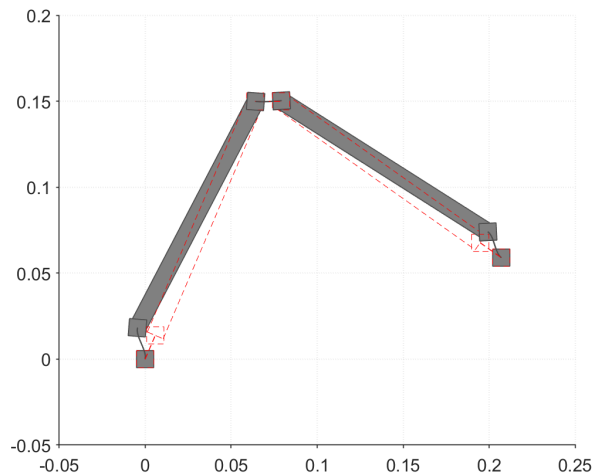


Figure 42: Mode shape 2 at 132.9 Hz in reference position

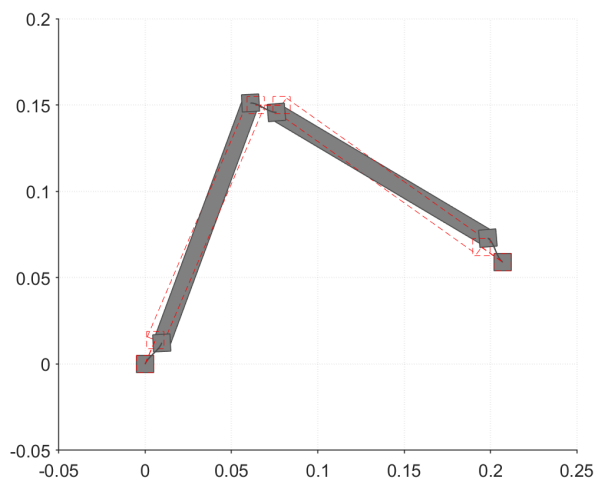


Figure 43: Mode shape 3 at 150.7 Hz in reference position

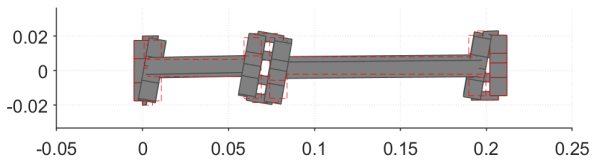


Figure 44: Mode shape 4 at 605.4 Hz in reference position

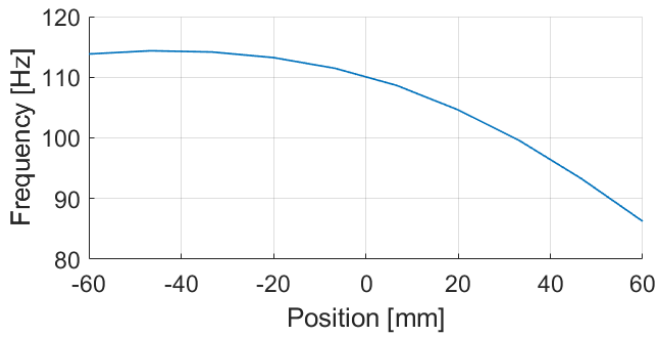


Figure 45: First parasitic eigenfrequency as a function of the position

E Pictures of the Test Setups

Appendix E provides photographs of the test setups used for the validation.



Figure 46: Arc setup encoder side

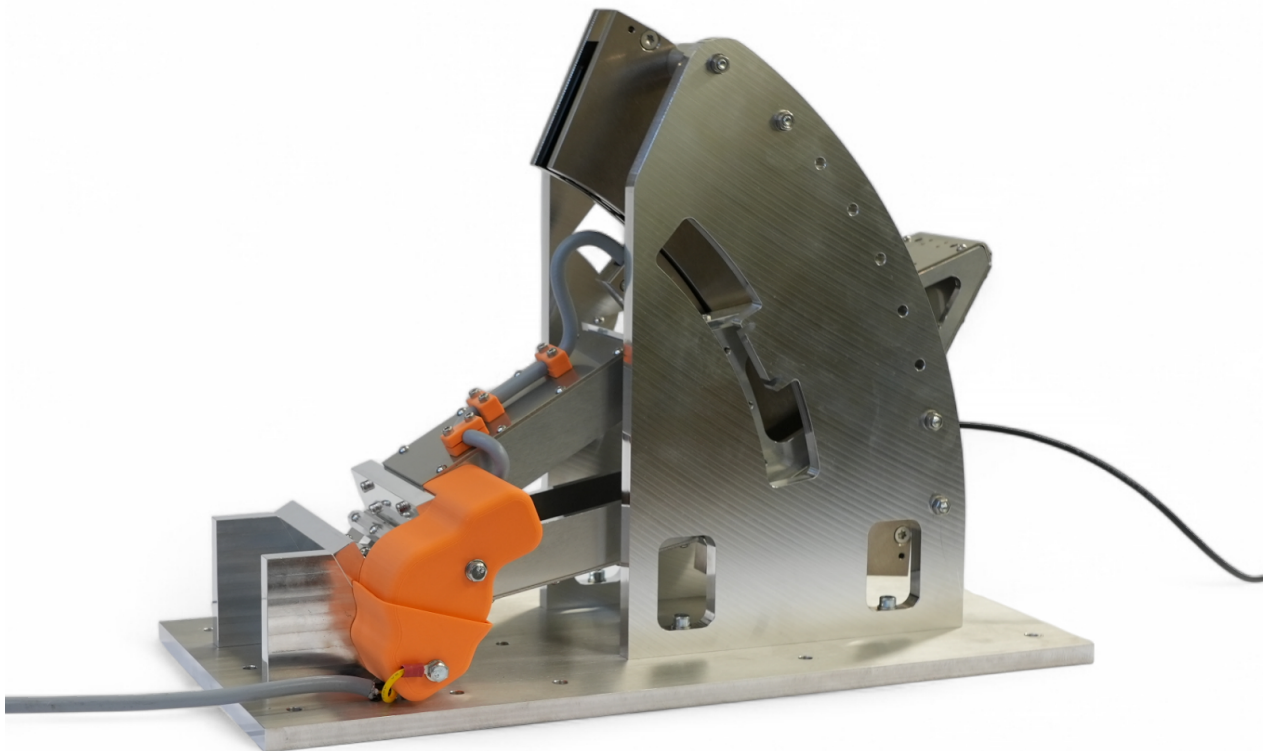
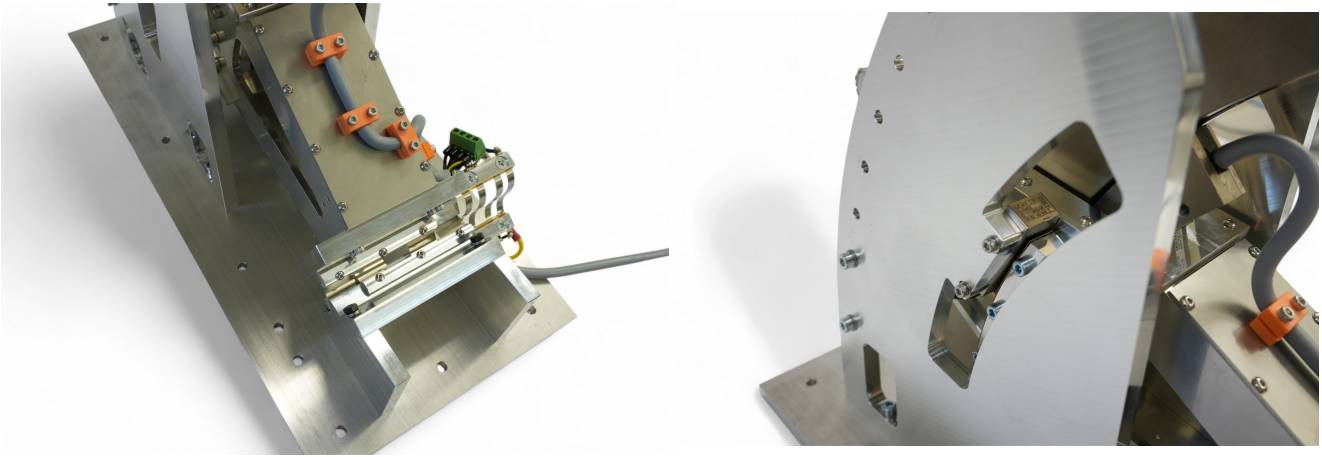


Figure 47: Arc setup with protective cover on cable routing



(a) Base flexure and cable routing

(b) Encoder location

Figure 48: Detail views arc setup

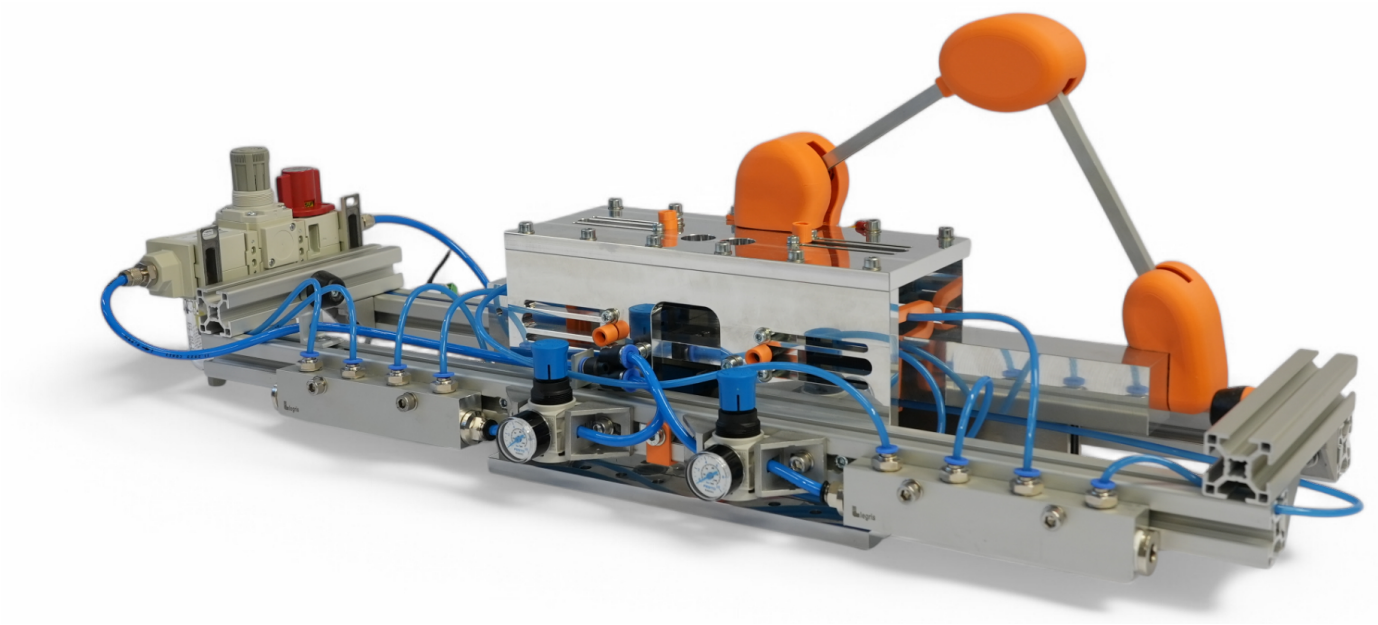
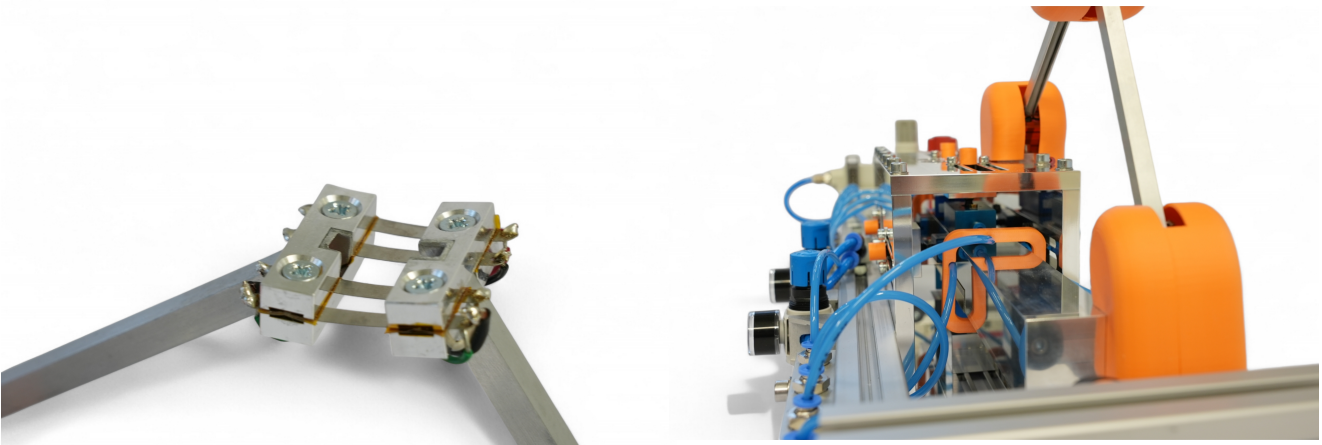


Figure 49: Linear setup



(a) Cable guide with protective cover removed

(b) Side view

Figure 50: Detail views linear setup

